Pharmacokinetic-rate images of indocyanine green for breast tumors using near-infrared optical methods

Burak Alacam[1]**, Birsen Yazici**[1,2]**, Xavier Intes**[2]**, Shoko Nioka**[3] **and Britton Chance**[3]

[1] Department of Electrical, Computer, and Systems Engineering, Rensselaer Polytechnic Institute, Troy, NY, USA
[2] Department of Biomedical Engineering, Rensselaer Polytechnic Institute, Troy, NY, USA
[3] Department of Biophysics and Biochemistry, University of Pennsylvania, PA, USA

E-mail: yazici@ecse.rpi.edu

Abstract

In this paper, we develop a method of forming pharmacokinetic-rate images of indocyanine green (ICG) and apply our method to *in vivo* data obtained from three patients with breast tumors. To form pharmacokinetic-rate images, we first obtain a sequence of ICG concentration images using the differential diffuse optical tomography technique. We next employ a two-compartment model composed of plasma, and extracellular–extravascular space (EES), and estimate the pharmacokinetic rates and concentrations in each compartment using the extended Kalman filtering framework. The pharmacokinetic-rate images of the three patient show that the rates from the tumor region and outside the tumor region are statistically different. Additionally, the ICG concentrations in plasma, and the EES compartments are higher around the tumor region agreeing with the hypothesis that around the tumor region ICG may act as a diffusible extravascular flow in compromised capillary of cancer vessels. Our study indicates that the pharmacokinetic-rate images may provide superior information than single set of pharmacokinetic rates estimated from the entire breast tissue for breast cancer diagnosis.

(Some figures in this article are in colour only in the electronic version)

1. Introduction

Near-infrared (NIR) diffuse optical imaging offers several advantages over other imaging modalities (Arridge 1999, Boppart *et al* 2004, Gu *et al* 2004, Intes and Chance 2005, Mahmood *et al* 1999, Sevick-Muraca *et al* 1997, Yodh and Chance 1995). NIR techniques are minimally invasive, easy to use, relatively inexpensive and can be made portable. Moreover, optical

techniques, when coupled with contrast agents, have the potential to provide molecular/cellular level information, which can improve cancer detection, staging and treatment monitoring (Alacam *et al* 2006, Cuccia *et al* 2003, Intes *et al* 2003, Mahmood *et al* 1999, Sevick-Muraca *et al* 1997).

Among many commercially available optical contrast agents, only indocyanine green (ICG) is approved for use in humans by the Food and Drug Administration (ElDeosky *et al* 1999, Hansen *et al* 1993, Shinohara *et al* 1996). ICG is a blood pooling agent that has different delivery behavior between normal and cancer vasculature. In normal tissue, ICG acts as a blood flow indicator in tight capillaries of normal vessels. However in tumors, ICG may act as a diffusible (extravascular) flow in leaky capillary of vessels (Alacam *et al* 2006, Cuccia *et al* 2003, Ntziachristos *et al* 2000, Vaupel *et al* 1991). Therefore, pharmacokinetics of ICG has the potential to provide new tools for tumor detection, diagnosis and staging.

One approach to analyze pharmacokinetics of contrast agents is the compartmental modeling (Anderson 1983, Jacquez 1972, Tornoe 2002). A number of studies using compartmental modeling were reported to show the feasibility of ICG pharmacokinetics in tumor characterization (Alacam *et al* 2006, Cuccia *et al* 2003, Intes *et al* 2003). Cuccia *et al* (2003) presented a study of the dynamics of ICG in an adenocarcinoma rat tumor model using a two-compartment model. Intes *et al* (2003) presented the uptake of ICG in breast tumors using a continuous wave diffuse optical tomography apparatus using a two-compartment model. We recently introduced the extended Kalman filtering (EKF) framework to model and estimate the ICG pharmacokinetics and tested three different compartmental models for the ICG pharmacokinetics using the *in vivo* NIR data collected from Fischer rats with cancerous tumors (Alacam *et al* 2006). Our study suggests that the pharmacokinetic rates out of the vasculature are higher in edematous tumors as compared to necrotic tumors.

In all the studies described above, the pharmacokinetic rates are assumed to be constant over a tissue volume that may be as large as the entire imaging domain. However, pharmacokinetic rates are expected to be different in healthy and tumor tissue as reported in positron emission tomography (PET) and magnetic resonance imaging (MRI) literature. It was shown that the spatially resolved pharmacokinetic-rate analysis provides increased sensitivity and specificity for breast cancer diagnosis (Mussurakis *et al* 1997, Su *et al* 2005, Sun *et al* 2006). For example, Sun *et al* (2006) showed that FAU (1-2′-deoxy-2′-fluoro- β-D-arabinfuranosyl urasil, a PET contrast agent) accumulation in tumor regions is significantly higher when compared to normal breast tissue based on pharmacokinetic-rate images. Mussurakis *et al* (1997) showed that the pharmacokinetics of gadolinium-DTPA (an MRI contrast agent) can be used to differentiate between malignant and benign breast tumors with a high accuracy. It has also been shown that the spatially resolved image interpretation is superior to the isolated use of quantitative pharmacokinetic rates.

In the area of diffuse NIR spectroscopy and imaging, a number of studies on spatially resolved pharmacokinetic rates has been reported (Gurfinkel *et al* 2000, Milstein *et al* 2005). Gurfinkel *et al* (2000) presented *in vivo* NIR reflectance images of ICG pharmacokinetics to discriminate canine adenocarcinoma (located at 0.5–1 cm depth) from normal mammary tissue. These images were generated by a non-tomographic technique using a CCD camera that is suitable only for imaging tumors close to surface. Milstein *et al* (2005) presented a Bayesian tomographic image reconstruction method to form pharmacokinetic-rate images of optical fluorophores based on fluorescence diffuse optical tomography. Numerical simulations show that the method provides good contrast. However, no real data experiments were presented to study the diagnostic value of spatially resolved pharmacokinetic rates.

In this paper, we present a method of forming pharmacokinetic-rate images and report spatially resolved pharmacokinetic rates of ICG using *in vivo* NIR data acquired from three

patients with breast tumors. To the best of our knowledge, our work is the first study presenting the pharmacokinetic-rate images of an optical contrast agent using *in vivo* breast data based on tomographic techniques. We first develop a set of spatio-temporally resolved ICG concentration images based on differential diffuse optical tomography. We model the ICG pharmacokinetics by a two-compartment model composed of plasma and extracellular–extravascular space (EES) compartments. We then estimate the ICG pharmacokinetic rates and the concentrations in different compartments based on the EKF framework (Alacam *et al* 2006). We show that the pharmacokinetic rates from the tumor region and outside the tumor region are statistically different. We also estimate a single set of pharmacokinetic rates (bulk pharmacokinetic rates) for the entire breast tissue. Our study indicates that spatially resolved pharmacokinetic rates provide more consistent and superior diagnostic information as compared to the bulk pharmacokinetic rates.

The rest of the paper is organized as follows. In section 2, we present the reconstruction of ICG concentration images. In section 3, we present modeling and estimation of ICG pharmacokinetic-rate images using the EKF framework. In section 4, we present the spatially resolved ICG pharmacokinetic-rate analysis of *in vivo* breast data. Section 5 summarizes our results and conclusion.

2. Reconstruction of bulk ICG concentration images

In our data collection process, a sequence of boundary measurements are collected over a period of time. Each set of measurements are used to form a frame of the ICG concentration images. The resulting sequence of ICG concentration images are then used to form pharmacokinetic-rate images. To reconstruct each frame of the ICG concentration images, we follow a static reconstruction approach and use differential diffuse optical tomography (DDOT) technique (Intes *et al* 2003, Ntziachristos *et al* 1999).

In DDOT, two sets of excitation measurements are collected corresponding to before and after the ICG injection, and the ICG concentration is determined by the perturbation method (Intes *et al* 2003, Ntziachristos *et al* 1999). The photon propagation before and after the injection is modeled by the following diffusion equations:

$$\nabla \cdot D_x(r)\nabla \Phi_x^{\pm}(r, \omega) - \left(\mu_{ax}^{\pm}(r) + j\omega/c\right)\Phi_x^{\pm}(r, \omega) = 0, \qquad r \in \Omega \subset R^3, \tag{1}$$

with Robin-type boundary conditions:

$$2D_x(r)\frac{\partial \Phi_x^{\pm}(r, \omega)}{\partial \nu} + \rho \Phi_x^{\pm}(r, \omega) = -S(r, \omega), \qquad r \in \partial\Omega, \tag{2}$$

where x stands for the excitation, c is the speed of light inside the medium Ω; ω denotes the modulation frequency of the source, $\mu_{ax}^{-}(r)$ and $\mu_{ax}^{+}(r)$ are the absorption coefficients before and after the ICG injection, D_x is the diffusion coefficient which is assumed independent of $\mu_{ax}^{\pm}$, known but not necessarily constant, $\Phi_x^{\pm}(r, \omega)$ denotes optical field at location r before and after the ICG injection. Here, ν denotes the outward normal to the boundary $\partial\Omega$ of Ω, ρ is a constant representing the refractive index mismatch between the two regions separated by $\partial\Omega$ and $S(r, \omega)$ is the excitation source on the boundary.

The absorption coefficients after the injection μ_{ax}^{+} are modeled as a sum of the absorption coefficient of the medium before the ICG injection μ_{ax}^{-} and the perturbation caused by the ICG $\Delta\mu_{ax}(r)$:

$$\Delta\mu_{ax}(r) = \mu_{ax}^{+}(r) - \mu_{ax}^{-}(r), \qquad r \in \Omega \subset R^3. \tag{3}$$

In the forward model, the analytical solutions of the heterogonous diffusion equation given in (1) is derived using first-order Rytov approximation (Intes *et al* 2003). The sample volume

is divided into a set of voxels and the measurements are related to the relative absorption coefficients of each voxel by a system of linear equations. The shape of the breast was approximated as a cylinder and the Kirchhoff approximation (Ripoll *et al* 2001a, 2001b) for diffuse waves was used to model the interaction of light with boundaries. In order to minimize optode-tissue coupling mismatch due to breathing motion, the forward model was augmented with the coupling coefficient technique as described in Boas *et al* (2001).

Here, the Rytov-type measurements, which are defined by the natural logarithm of the ratio of the post-ICG measurements to the pre-ICG measurements were used (Ntziachristos *et al* 1999). Let $\Psi_x(\omega; r_d; r_s)$ denote the Rytov-type measurements at location r_d due to source at r_s. The linearized relationship between the differential absorption coefficient and measurements is given by O'Leary (1996)

$$\Psi_x(\omega; r_d; r_s) = -\frac{1}{\Phi_x^-(\omega; r_d; r_s)} \int_\Omega G_x^-(r, \omega; r_d) I_x(r) \Phi_x^-(r, \omega; r_s) \, \mathrm{d}^3 r, \tag{4}$$

where $\Phi_x^-(r, \omega; r_s)$ is the photon density obtained at the excitation wavelength before ICG injection, $I_x(r) = c\Delta\mu_{ax}(r)/D_x$, and $G_x^-(r, \omega; r_d)$ is the Green's function of (1) for a source at r_s before the injection.

We address the inverse problem of recovering $\Delta\mu_{ax}$ from Rytov measurements Ψ_x based on the forward model (4) using the singular-value decomposition of the Moore–Penrose generalized system. We use a zeroth-order Tikhonov regularization to stabilize the inversion procedure. The regularization parameter was determined by *L*-curve analysis (Hansen and O'Leary 1993) using the data obtained from a phantom study previously employed to validate the apparatus (Intes *et al* 2003). The optimal regularization parameter was found to be 6×10^{-4} and set to be the same for all patient images and time instances. A detailed discussion of the forward and inverse models used for the reconstruction of differential absorption coefficients ($\Delta\mu_{ax}$) can be found in Intes *et al* (2003).

To construct a set of ICG concentration images, we use the linear relationship between the differential absorption coefficients and ICG concentrations (Landsman *et al* 1976),

$$\Delta\mu_a(r) = \ln 10 \epsilon_\lambda m(r), \tag{5}$$

where ϵ_λ is the extinction coefficient of ICG at the wavelength 805 nm, $m(r)$ is the bulk ICG concentration in the tissue and $\Delta\mu_a(r)$ is as defined in (3).

Note that the method described here is applicable for frequency domain case but for simplicity we set the frequency to zero, i.e. $\omega = 0$.

3. Modeling and estimation of ICG pharmacokinetics

3.1. Two-compartment model of ICG pharmacokinetics

Using the method outlined in section 2, we reconstruct a sequence of ICG concentration images. As an example, figures 1–3 show a set of images reconstructed from *in vivo* breast data.

Our objective is to model the pharmacokinetics of ICG at each voxel of ICG concentration images using compartmental modeling. To do so, we first extracted the time varying ICG concentration curves for each voxel from the sequence of ICG concentration images. An example of such a curve is shown in figure 4. We next fit a two-compartment model to each ICG concentration curve (Alacam *et al* 2006, Gurfinkel *et al* 2000).
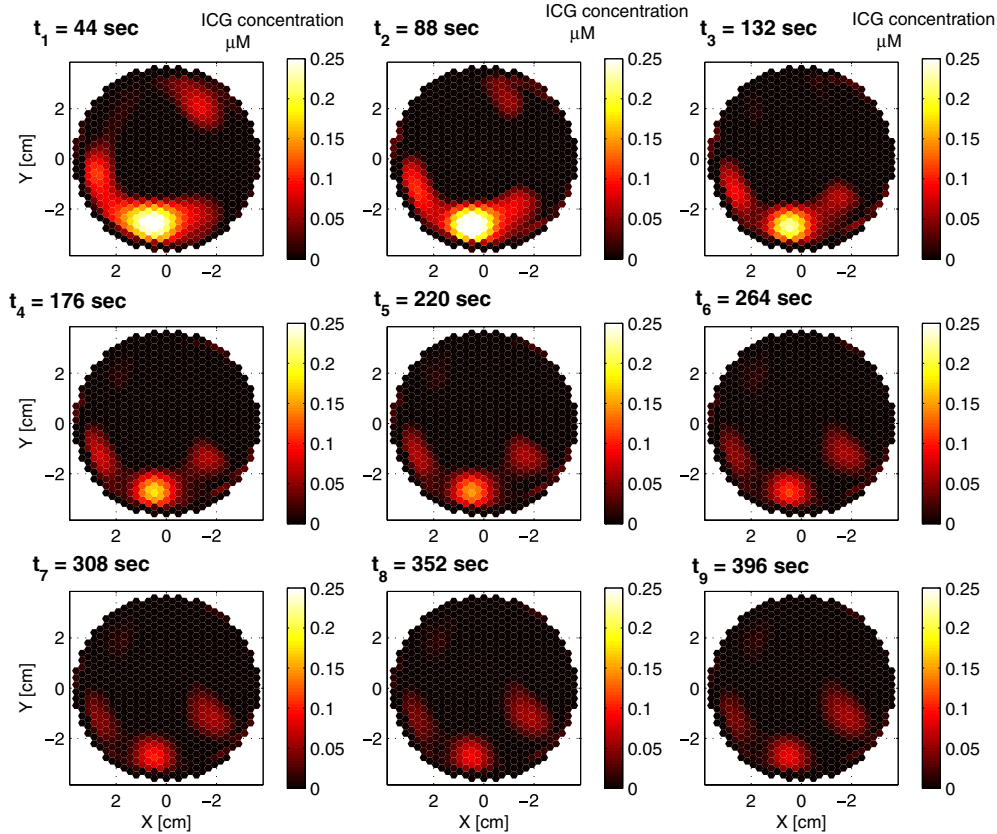
Figure 1. ICG concentration images for a set of time instants for case 1.

Using the two-compartment model introduced by Alacam *et al* (2006), ICG transition between plasma and extracellular–extravascular space (EES) can be modeled as follows:

$$\begin{bmatrix} \dot{C}_e(t) \\ \dot{C}_p(t) \end{bmatrix} = \begin{bmatrix} -k_{\text{out}} & k_{\text{in}} \\ k_{\text{out}} & -(k_{\text{in}} + k_{\text{elm}}) \end{bmatrix} \begin{bmatrix} C_e(t) \\ C_p(t) \end{bmatrix} + \omega(t), \qquad t \in [T_0, T_1], \tag{6}$$

where $C_p(t)$ and $C_e(t)$ represent the ICG concentrations in plasma and EES at time t, respectively. The rates $k_{\text{in}}, k_{\text{out}}$ and k_{elm} have a unit of sec^{-1}. They are defined as the permeability surface area products given by $PS\gamma$, where P is the capillary permeability constant, S is the capillary surface area and γ is the tissue density. k_{in} and k_{out} govern the leakage into and the drainage out of the EES. The parameter k_{elm} describes the ICG elimination from the body through kidneys and liver. Here, $\omega(t)$ is uncorrelated zero-mean Gaussian process with covariance matrix $\mathbf{Q}$ representing the model mismatch.

The actual total ICG concentration in the tissue is a linear combination of plasma and the EES ICG concentrations, and modeled as

$$m(t) = \begin{bmatrix} v_e & v_p \end{bmatrix} \begin{bmatrix} C_e(t) \\ C_p(t) \end{bmatrix} + \eta(t), \qquad t \in [T_0, T_1], \tag{7}$$

where $m(t), C_e(t)$ and $C_p(t)$ are defined in (5) and (6), v_p and v_e are plasma and the EES volume fractions, respectively, and $\eta(t)$ is uncorrelated zero-mean Gaussian process with covariance matrix $\mathbf{R}$, representing the measurement noise.
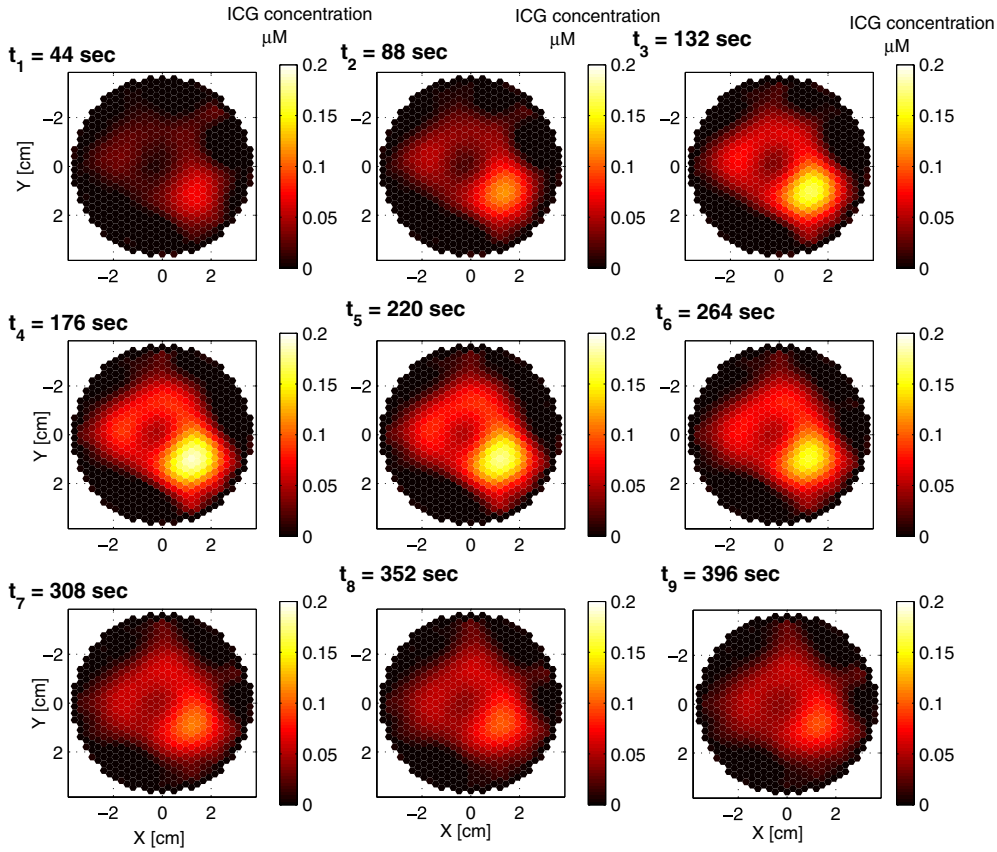
Figure 2. ICG concentration images for a set of time instants for case 2.

3.2. Estimation of ICG pharmacokinetics using extended Kalman filtering

In matrix–vector notation, (6) and (7) can be expressed as

$$\dot{\mathbf{C}}(t) = \mathbf{K}(\boldsymbol{\alpha})\mathbf{C}(t) + \boldsymbol{\omega}(t), \qquad m(t) = \mathbf{V}(\boldsymbol{\alpha})\mathbf{C}(t) + \eta(t), \tag{8}$$

where $\mathbf{C}(t)$ denotes the concentration vector with elements $C_e(t)$, and $C_p(t)$; $\mathbf{K}(\boldsymbol{\alpha})$ is the system matrix, $\mathbf{V}(\boldsymbol{\alpha})$ is the measurement matrix as defined in equation (7) and $\boldsymbol{\alpha}$ is the parameter vector given by

$$\boldsymbol{\alpha} = [k_{\text{out}} \quad k_{\text{in}} \quad k_{\text{elm}} \quad v_e \quad v_p]^T. \tag{9}$$

The ICG measurements in (8) are collected at discrete time instances, $t = kT, k = 0, 1, \ldots$, where T is the sampling period. Therefore, the continuous model described in (8) is discretized. We can express the discrete compartmental model as follows:

$$\mathbf{C}_d(k+1) = \mathbf{K}_d(\boldsymbol{\theta})\mathbf{C}_d(k) + \boldsymbol{\omega}_d(k), \qquad \mathbf{m}(k) = \mathbf{V}_d(\boldsymbol{\theta})\mathbf{C}_d(k) + \boldsymbol{\eta}_d(k), \tag{10}$$

where $\mathbf{K}_d(\boldsymbol{\theta}) = e^{\mathbf{K}(\boldsymbol{\alpha})}$ is the discrete time system matrix; $\mathbf{V}_d(\boldsymbol{\theta}) = \mathbf{V}(\boldsymbol{\alpha})$ is the discrete measurement matrix; $\boldsymbol{\omega}_d(k)$ and $\boldsymbol{\eta}_d(k)$ are zero-mean Gaussian white noise processes with covariances matrix $\mathbf{Q}_d$ and variance $\mathbf{R}_d$, respectively. The vector $\boldsymbol{\theta}$ is composed of parameters τ_{ij} which are functions the pharmacokinetic rates and volume fractions:

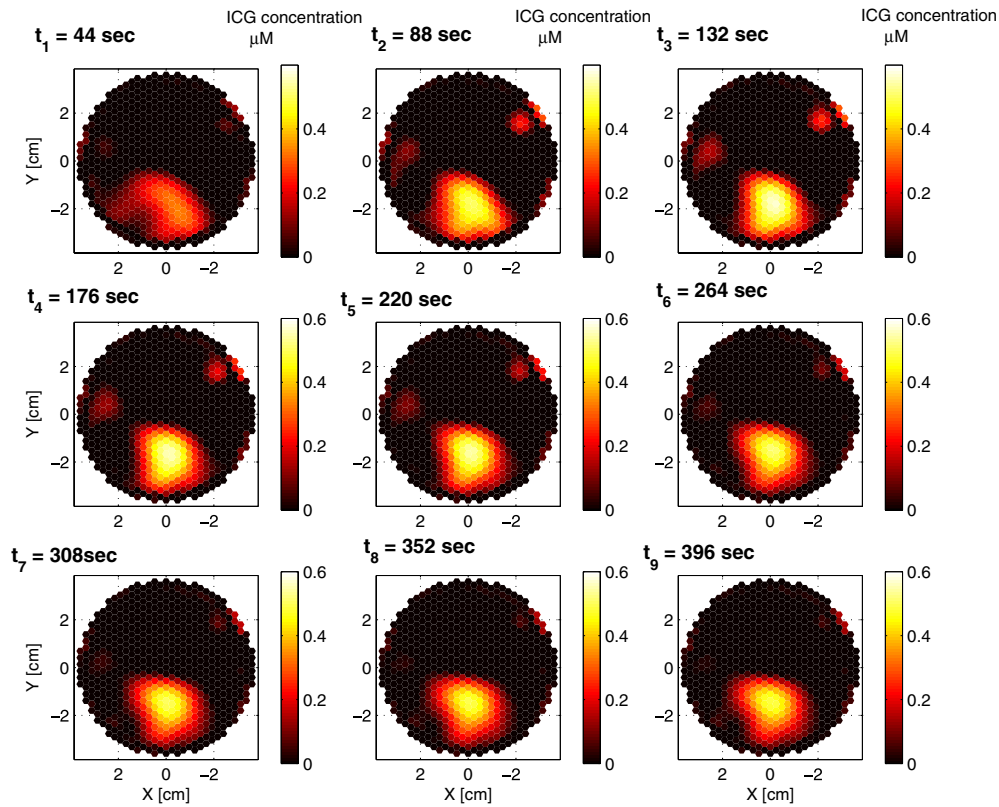$$\boldsymbol{\theta} = [\tau_{11} \quad \tau_{12} \quad \tau_{21} \quad \tau_{22} \quad v_e \quad v_p]^T. \tag{11}$$

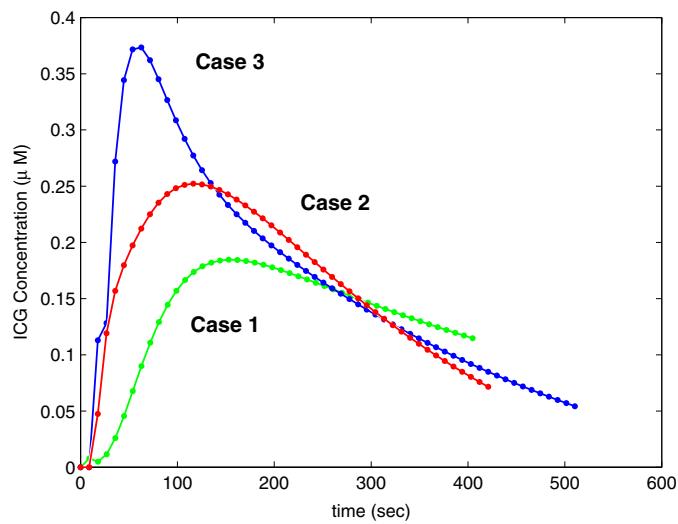**Figure 3.** ICG concentration images for a set of time instants for case 3.

Figure 4. Time course of ICG concentration curves for a specific voxel, 65th, 276th, 188th voxel for cases 1, 2 and 3, respectively.
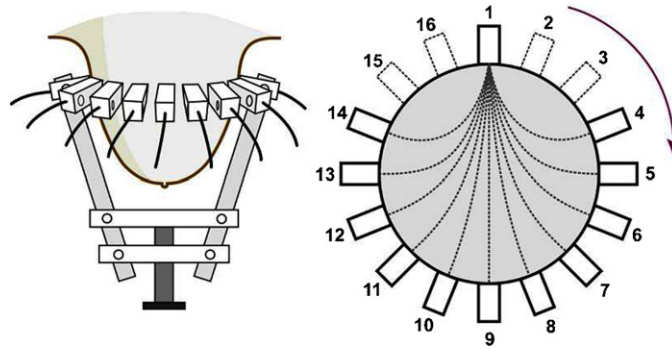
Figure 5. (Left) Schematic diagram. (Right) The cut section of the CW NIR imaging apparatus with 16 sources and detectors.

We first estimate τ_{ij}, $i, j = 1, 2$ and then compute the pharmacokinetic rates k_{in}, k_{out} and k_{elm} (Alacam *et al* 2006, Chen 1999). The explicit form of the discrete state-space model is given as follows:

$$\begin{bmatrix} C_e(k+1) \\ C_p(k+1) \end{bmatrix} = \begin{bmatrix} \tau_{11} & \tau_{12} \\ \tau_{21} & \tau_{22} \end{bmatrix} \begin{bmatrix} C_e(k) \\ C_p(k) \end{bmatrix} + \omega_d(k)$$

$$m(k) = \begin{bmatrix} v_e & v_p \end{bmatrix} \begin{bmatrix} C_e(k) \\ C_p(k) \end{bmatrix} + \eta_d(k). \tag{12}$$

We estimate the parameter vector $\boldsymbol{\theta}$ and concentration vector $\mathbf{C}_d$ by using the EKF framework. The EKF is a recursive modeling and estimation method with numerous advantages in ICG pharmacokinetic modeling (Alacam *et al* 2006). These include effective modeling of multiple compartments, and multiple measurement systems in the presence of measurement noise and uncertainties in the compartmental model dynamics, simultaneous estimation of model parameters and ICG concentrations in each compartment, statistical validation of estimated concentrations and error bounds on the model parameter estimates, and incorporation of available a priori information about the initial conditions of the permeability rates into the estimation procedure.

When both states (ICG concentrations) and model parameters (pharmacokinetic rates and volume fractions) are unknown, a linear state-space model can be regarded as a nonlinear model; the linear system parameters and states combine to form the new states of the nonlinear model. This system is then linearized and the new unknown states are found using the EKF estimator (Alacam *et al* 2006, Ljung 1979, Togneri and Deng 2003, Nelson and Stear 1976). In EKF framework, $\boldsymbol{\theta}$ can be treated as a random process with the following model:

$$\boldsymbol{\theta}(k+1) = \boldsymbol{\theta}(k) + \varsigma_d(k), \tag{13}$$

where $\varsigma_d(k)$ is a zero-mean Gaussian process with covariance matrix $\mathbf{S}_d$.

Table 1 summarizes the joint estimation of pharmacokinetic rates and ICG concentration in different compartments. In table 1, $\hat{\mathbf{C}}_d(k|k-1)$ is the state estimate propagation at step k given all the measurements up to step $k-1$, $\hat{\mathbf{C}}_d(k)$ is the state estimate update at step k, $\mathbf{P}_{k,k-1}$ denotes the error covariance propagation at step k given all the measurements up to step $k-1$, $\mathbf{P}_{k,k}$ is the error covariance update at step k, $\mathbf{S}_d$ is the preassigned covariance matrix of $\varsigma_d(k)$, $\mathbf{J}_k$ is the Jacobian matrix due to iterative linearization of the state equation at step k, $\mathbf{G}_k$ is the recursive Kalman gain at step k, $\mathbf{R}_d$ is the covariance matrix of the measurements, $\mathbf{Q}_d$ is the covariance matrix of the concentration vector and $\mathbf{I}$ is the identity matrix. A detailed
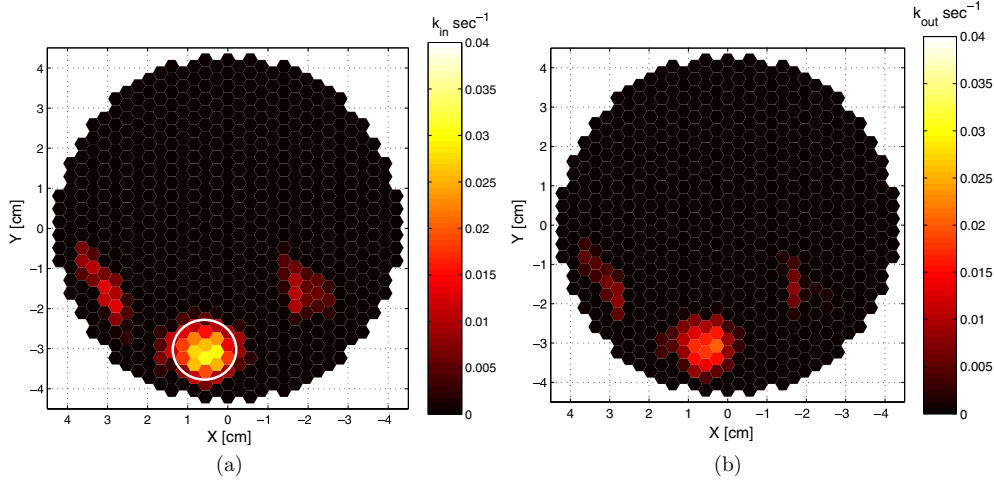
Figure 6. Pharmacokinetic rate images, (a) k_{in} and (b) k_{out} for case 1. The k_{in} images are shown with approximate tumor location and size.

Table 1. EKF algorithm for simultaneous estimation of states and parameters.

Initial conditions	$\begin{bmatrix} \hat{\mathbf{C}}_d(0) \\ \hat{\boldsymbol{\theta}}(0) \end{bmatrix} = \begin{bmatrix} E(\mathbf{C}_d(0)) \\ \hat{\boldsymbol{\theta}}(0) \end{bmatrix}, \mathbf{P}_{0,0} = \begin{bmatrix} Var(\mathbf{C}_d(0)) & 0 \\ 0 & \mathbf{S}_d \end{bmatrix}$
State estimate propagation	$\begin{bmatrix} \hat{\mathbf{C}}_d(k\|k-1) \\ \hat{\boldsymbol{\theta}}(k\|k-1) \end{bmatrix} = \begin{bmatrix} \mathbf{K}_d(\hat{\boldsymbol{\theta}}(k-1))\hat{\mathbf{C}}_d(k-1) \\ \hat{\boldsymbol{\theta}}(k-1) \end{bmatrix}$
Error covariance propagation	$\mathbf{P}_{k,k-1} = \mathbf{J}_{k-1}\mathbf{P}_{k-1,k-1}\mathbf{J}_{k-1}^T + \begin{bmatrix} \mathbf{Q}_d & 0 \\ 0 & \mathbf{S}_d \end{bmatrix}$
State estimate update	$\begin{bmatrix} \hat{\mathbf{C}}_d(k) \\ \hat{\boldsymbol{\theta}}(k) \end{bmatrix} = \begin{bmatrix} \hat{\mathbf{C}}_d(k\|k-1) \\ \hat{\boldsymbol{\theta}}(k\|k-1) \end{bmatrix}$ $+ \mathbf{G}_k(\mathbf{m}(k) - \mathbf{V}_d(\hat{\boldsymbol{\theta}}(k\|k-1))\hat{\mathbf{C}}_d(k\|k-1))$
Error covariance update	$\mathbf{P}_{k,k} = [\mathbf{I} - \mathbf{G}_k\Lambda_{k\|k-1}]\mathbf{P}_{k,k-1}$
Kalman gain	$\mathbf{G}_k = \mathbf{P}_{k,k-1}\Lambda_{k\|k-1}^T[\Lambda_{k\|k-1}\mathbf{P}_{k,k-1}\Lambda_{k\|k-1}^T + \mathbf{R}_d]^{-1}$
Definitions	$\mathbf{J}_k = \begin{bmatrix} \mathbf{K}_d(\hat{\boldsymbol{\theta}}(k)) & \frac{\partial}{\partial\boldsymbol{\theta}}[\mathbf{K}_d(\hat{\boldsymbol{\theta}}(k))\hat{\mathbf{C}}_d(k)] \\ \mathbf{0} & \mathbf{I} \end{bmatrix}$
	$\Lambda_{k\|k-1} = \begin{bmatrix} \mathbf{V}_d(\hat{\boldsymbol{\theta}}(k\|k-1)) \\ 0 \end{bmatrix}^T$

discussion of the extended Kalman filtering algorithm, and the initialization of the parameters, concentrations and covariance matrices can be found in Alacam *et al* (2006).

4. Spatially resolved ICG pharmacokinetic rate analysis of *in vivo* breast data

4.1. Apparatus

In this work, we use the data collected with a continuous wave (CW) NIR imaging apparatus. The apparatus has 16 light sources, which are tungsten bulbs with less than 1 W of output power. They are located on a circular holder at an equal distance from each other with 22.5°
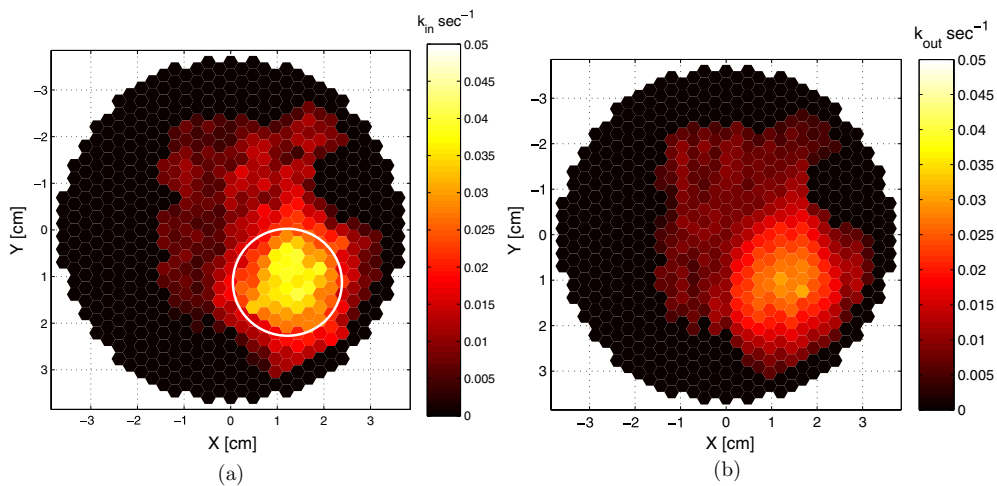
Figure 7. Pharmacokinetic-rate images, (a) k_{in} and (b) k_{out} for case 2. The k_{in} images are shown with approximate tumor location and size.
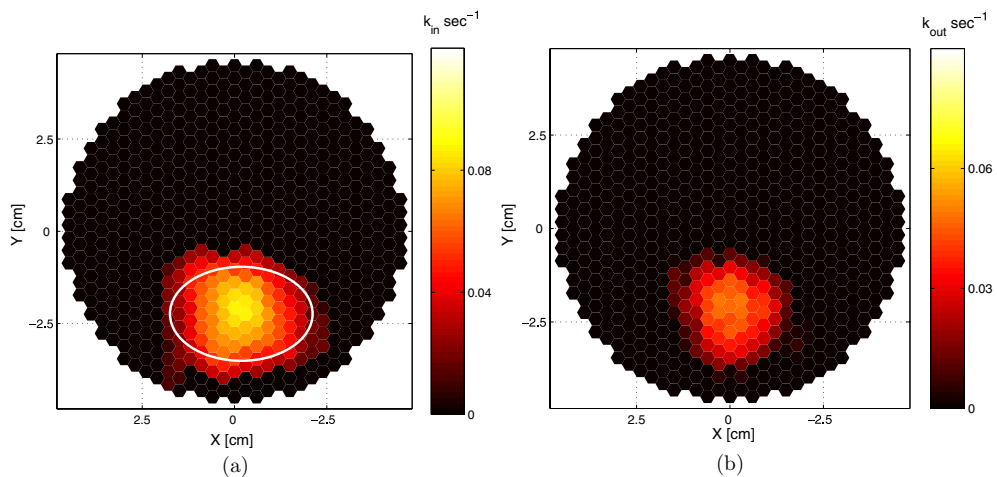

Figure 8. Pharmacokinetic-rate images, (a) k_{in} and (b) k_{out} for case 3. The k_{in} images are shown with approximate tumor location and size.

apart. Sixteen detectors, namely silicon photodiodes, are situated in the same plane. The breast is arranged in a pendular geometry with the source-detector probes gently touching its surface. Figure 5 illustrates the configuration of the apparatus and the configuration of the detectors and the sources in a circular plane. Note that sources and detectors are co-located. The detectors use the same positions as the sources to collect the light originating from one source at a time. Only the signals from the farthest 11 detectors are used in the analysis. For example, when source 1 is on, the data are collected using detectors 4–14. This provides sufficient number of source-detector readings (176 readings) to reconstruct $\Delta\mu_a$ images at each time instant. A band pass filter at 805 nm, the absorption peak of ICG, is placed in front of the sources to select the desired wavelength. A set of data for one source is collected every
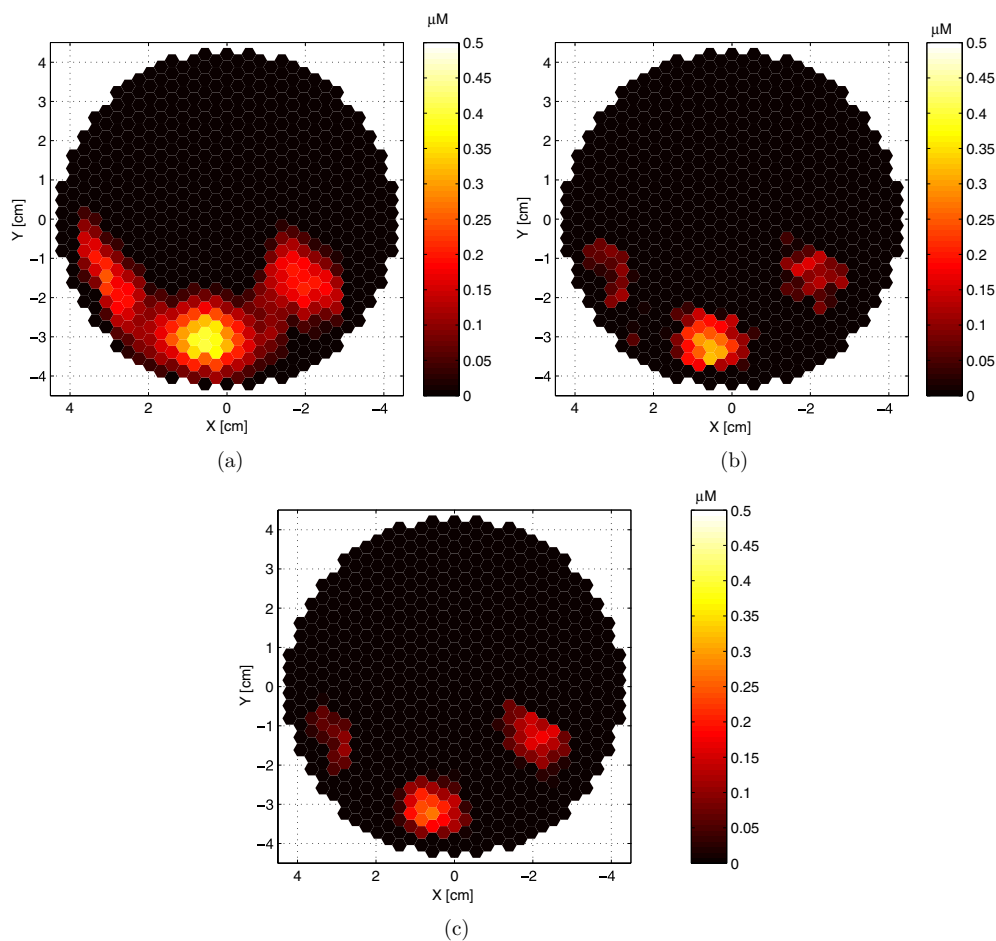
Figure 9. ICG concentration images in plasma for case 1 for (a) 246.4th, (b) 334.4th and (c) 422.4th s.

∼500 ms. The total time for a whole scan of the breast including 16 sources and 16 detectors is ∼8.8 s. A more detailed explanation of the apparatus and the data collection procedure can be found in (Nioka *et al* 1997).

4.2. Tumor information and protocol

Three different patients with different tumor types are included in this study. Measurements are made before the biopsy to avoid modification of the blood volume and flow in the tumor region. First case (case 1) is fibroadenoma, which corresponds to a mass estimated to be 1–2 cm in diameter within a breast of 9 cm diameter located at 6–7 o'clock. Second case (case 2) is adenocarcinoma corresponding to a tumor estimated to be 2–3 cm in diameter within a breast of 7.7 cm diameter located at 4–5 o'clock. The third case (case 3) is invasive ductal carcinoma, which corresponds to a mass estimated to be 4 cm by 3 cm located at 6 o'clock. Table 2 describes the tumor information for each patient. *A priori* information on the location and size of the tumor was obtained by palpation and the diagnostic information
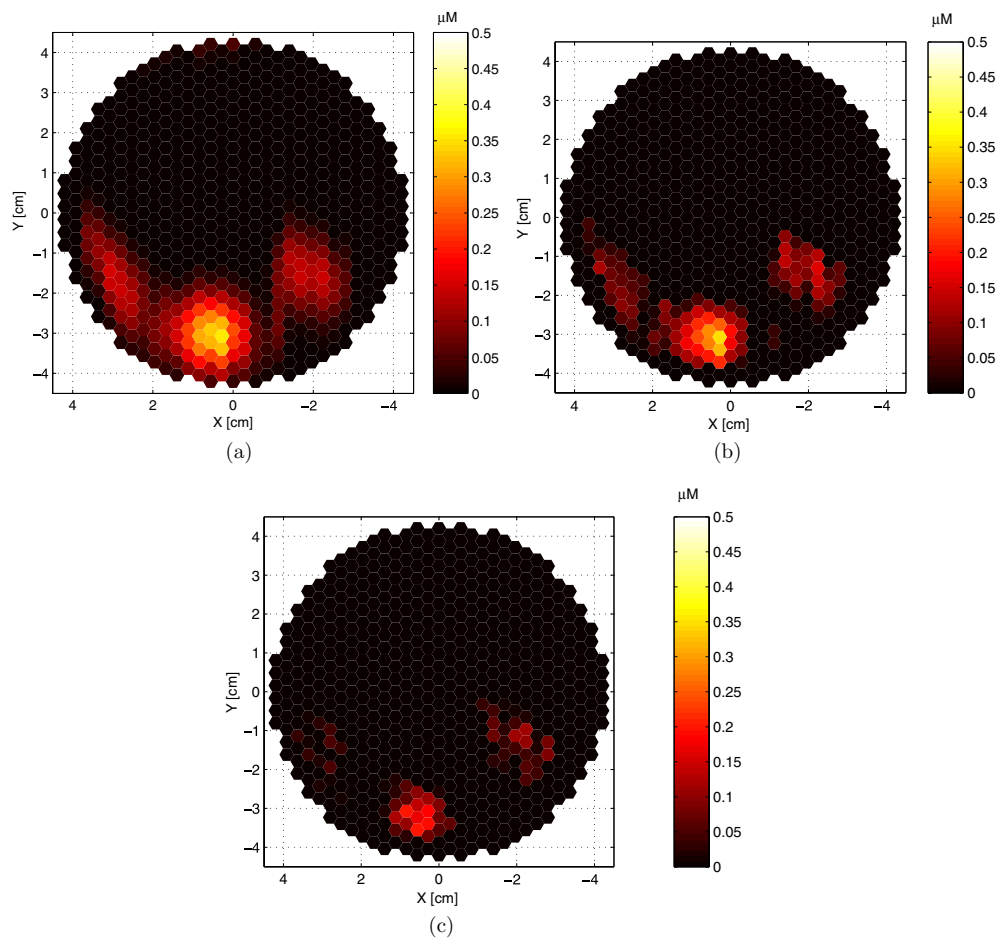
Figure 10. ICG concentration images in the EES for case 1 for (a) 246.4th, (b) 334.4th and (c) 422.4th s.

Table 2. Tumor information for each patient.

	Tumor type	Tumor size	Tumor location
Case 1	Fibroadenoma	1–2 cm	6–7 o'clock
Case 2	Adenocarcinoma	2–3 cm	4–5 o'clock
Case 3	Invasive ductal carcinoma	4 cm by 3 cm	6 o'clock

was derived *a posteriori* from biopsy and surgery. ICG is injected intravenously by bolus with a concentration of 0.25 mg kg^{-1} of body weight. Data acquisition started before the injection of ICG and continued for 10 min.

4.3. Results and discussion

Using the CW imager described above, source–detector readings were collected from different angles for each patient. Differential absorption coefficient images were reconstructed based
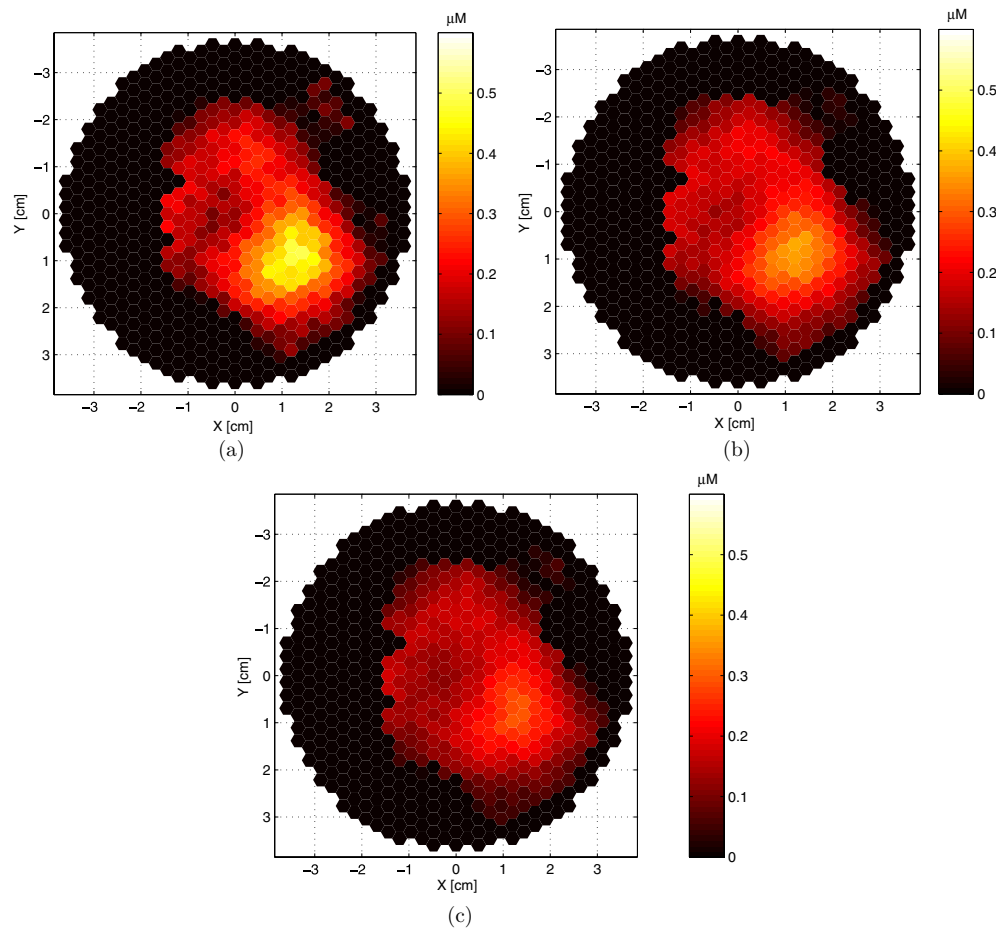
Figure 11. ICG concentration images in plasma for case 2 for (a) 228.8th, (b) 316.8th and (c) 404.8th s.

on DDOT forward model given in equations (1)–(4) with ω set to zero. Using the linear relationship (5) between ICG concentration and absorption coefficient, ICG concentration images were obtained for each case. A sample set of ICG concentration images for the selected time instants are shown in figures 1–3 for cases 1–3, respectively. Although only nine images are displayed, there are approximately 50 images for each case, each corresponding to a different time instant. Each image is composed of 649 voxels. Note that the ICG concentration images in figures 1–3 represent the bulk ICG concentrations in the tissue, not the ICG concentrations in plasma or the EES compartments.

We next extracted the time course of ICG concentration for each voxel. As an example, figure 4 shows the time course of ICG concentrations for all three cases for a specific voxel in the tumor region (65th, 276th, 188th voxel for cases 1, 2 and 3, respectively). We then fit the two-compartment model to each time course data using the EKF framework; and estimated k_{in}, k_{out}, k_{elm}, and the ICG concentrations in plasma and the EES. We chose initial values within the biological limits that lead to minimum norm error covariance matrix. The images of k_{in} and k_{out} for each case are shown in figures 6(a)–(b), and 7(a)–(b), 8(a)–(b), respectively. Additionally, we constructed the ICG concentration images for plasma and
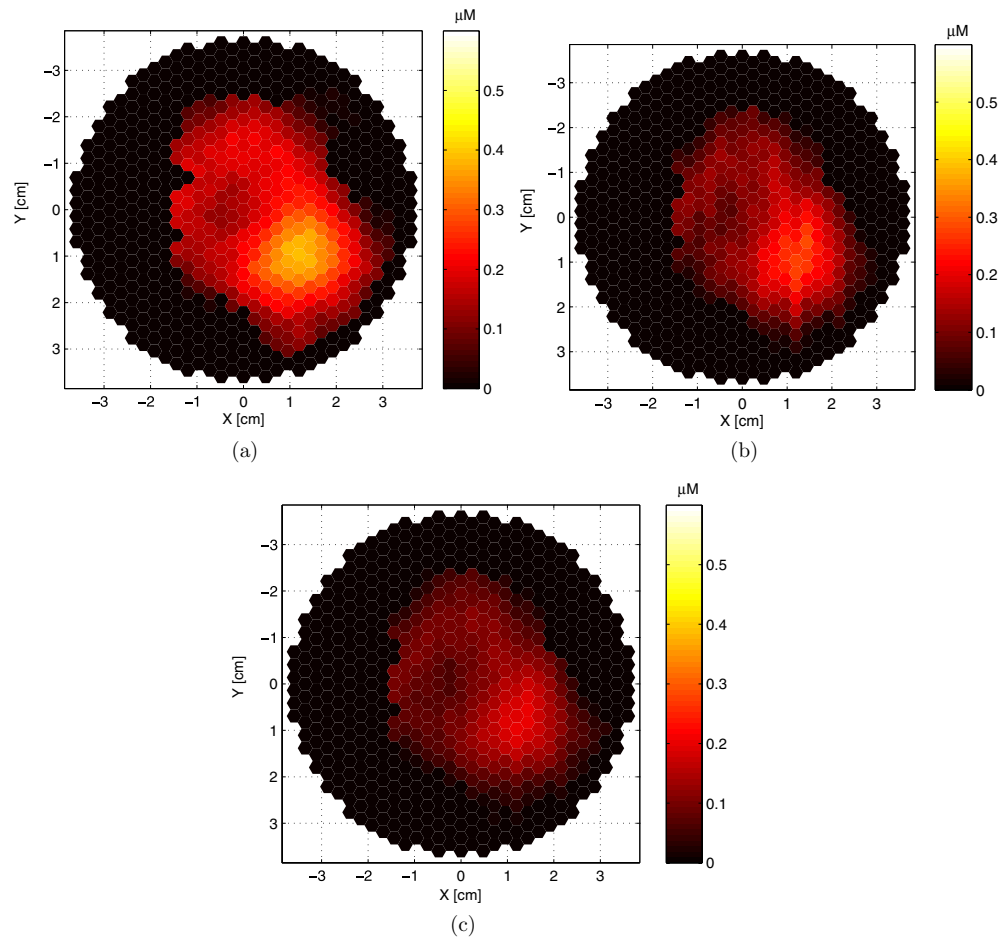
Figure 12. ICG concentration images in the EES for case 2 for (a) 228.8th, (b) 316.8th and (c) 404.8th s.

the EES compartments. Figures 9–14 show the ICG concentration in plasma and the EES for three different time instants for cases 1, 2 and 3, respectively. Our results show that the pharmacokinetic rates are higher around the tumor region agreeing with the fact that permeability increases around the tumor region due to compromised capillaries of tumor vessels. We also observed that ICG concentrations in plasma and the EES compartments are higher around the tumors agreeing with the hypothesis that around the tumor region ICG may act as a diffusible extravascular flow in leaky capillary of tumor vessels.

Using the *a priori* and *a posteriori* information on the location, and the size of the tumors, we plotted an ellipse (or a circle) to identify the approximate location and size of the tumor in the pharmacokinetic-rate images. We note that the radii of the ellipses were chosen large enough to include the tumor boundaries. Figures 6(a), 7(a) and 8(a) present the k_{in} images with approximate tumor location and size for cases 1, 2 and 3, respectively. The consistency of the bright regions in the k_{in} images, and circular/elliptical regions drawn based on the *a priori* and *a posteriori* information shows that the pharmacokinetic-rate images may provide good localization of tumors.
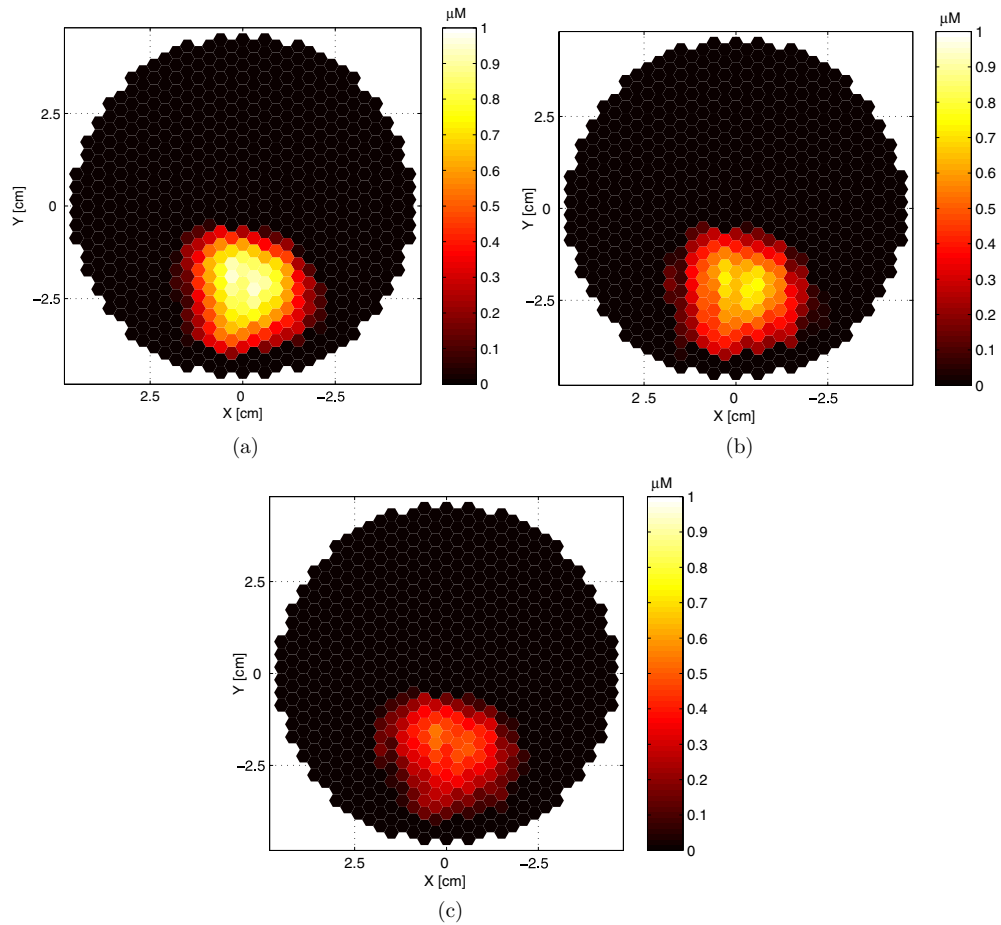
Figure 13. ICG concentration images in plasma for case 3 for (a) 246.4th, (b) 378.4th and (c) 510.4th s.

Table 3. Mean and standard deviation of pharmacokinetic rates for the tumor region and outside the tumor region.

	k_{in} (sec^{-1}10^{-2})		k_{out} (sec^{-1}10^{-2})		k_{elm} (sec^{-1}10^{-3})	
	Inside	Outside	Inside	Outside	Inside	Outside
Case 1	2.14 ± 0.018	0.73 ± 0.011	1.24 ± 0.069	0.43 ± 0.013	4.11 ± 0.057	3.87 ± 0.012
Case 2	2.92 ± 0.076	1.14 ± 0.052	1.58 ± 0.051	0.65 ± 0.036	3.94 ± 0.081	4.12 ± 0.047
Case 3	6.87 ± 0.093	3.06 ± 0.015	4.96 ± 0.048	1.66 ± 0.072	4.49 ± 0.056	4.46 ± 0.081

The histograms of k_{in} and k_{out} images for the tumor region (as indicated by circular/elliptical regions) and outside the tumor region are shown in figures 15(a)–(c) and figures 16(a)–(c), respectively. Note that all nonzero voxels outside the elliptical region constitute 'outside the tumor region'. The solid curves in figures 15 and 16 show the Gaussian fit. The histograms and their Gaussian fits in figures 15 and 16 show that the mean and the standard deviation of k_{in} and k_{out} values are different for the tumor and outside the tumor region. Table 3 tabulates the mean values ($\pm$ spatial standard deviation) of the pharmacokinetic rates
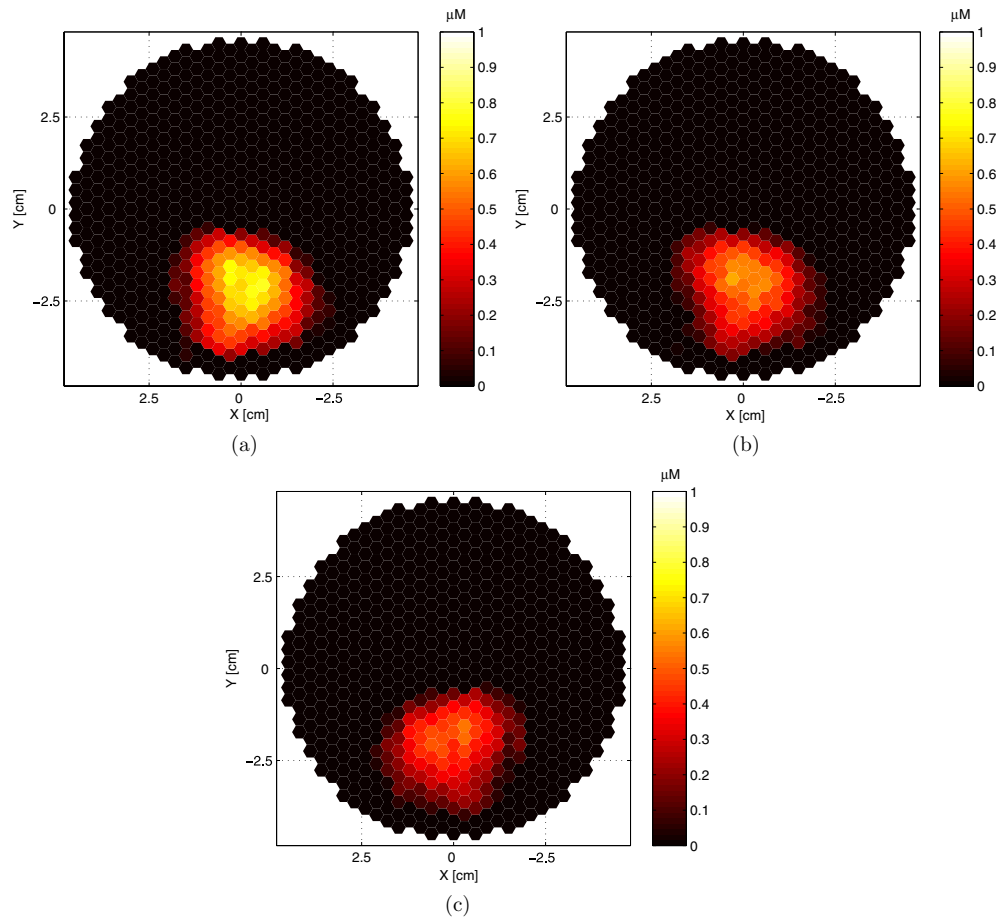
Figure 14. ICG concentration images in the EES for case 3 for (a) 246.4th, (b) 378.4th and (c) 510.4th s.

Table 4. Bulk pharmacokinetic rates extracted from the entire breast tissue.

	k_{in} (sec^{-1}10^{-2})	k_{out} (sec^{-1}10^{-2})	k_{elm} (sec^{-1}10^{-3})
Case 1	0.84 ± 0.013	0.62 ± 0.017	3.66 ± 0.042
Case 2	2.01 ± 0.022	0.83 ± 0.012	4.01 ± 0.054
Case 3	4.06 ± 0.072	3.36 ± 0.051	4.37 ± 0.052

for the tumor region and outside the tumor region for all three cases. The pharmacokinetic rates are higher for case 3 (invasive ductal carcinoma), for both the tumor region and outside the tumor region as compared to case 2 (adenocarcinoma). Similarly, the kinetic rates are higher for case 2 (adenocarcinoma), as compared to case 1 (fibroadenoma) for both the tumor region and outside the tumor region. This observation shows that high mean values of k_{in} and k_{out} may be indicative of tumor aggressiveness.

To understand the value of pharmacokinetic rate imaging as compared to the bulk pharmacokinetic rate analysis, we averaged the concentration images spatially, and obtained
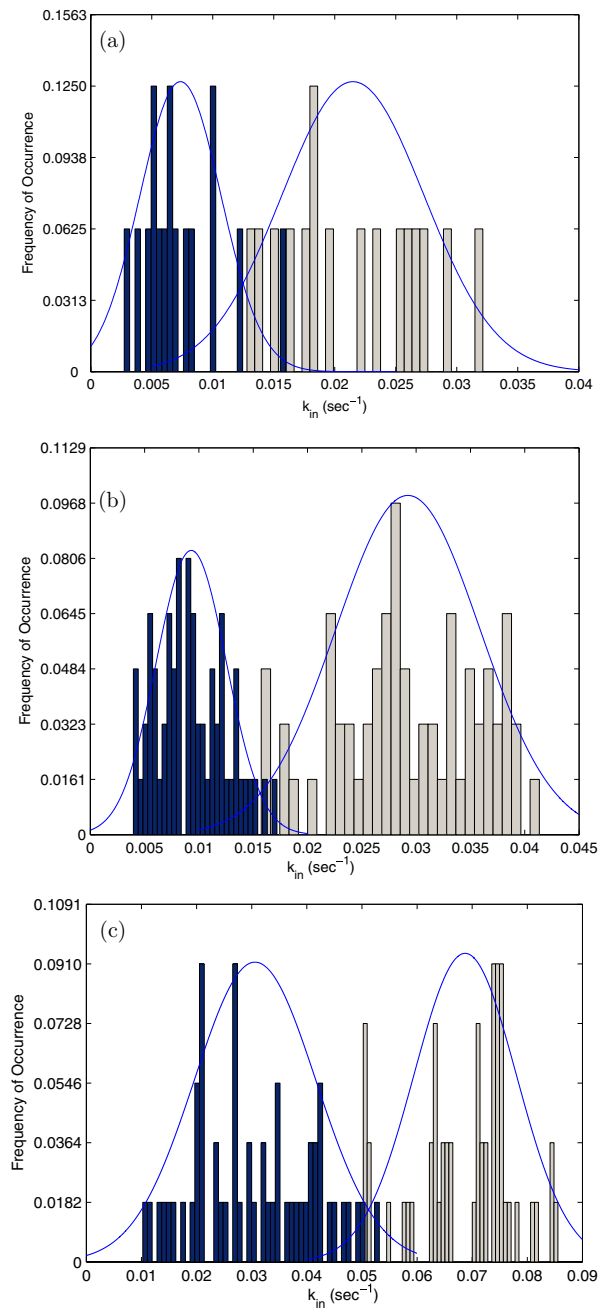
Figure 15. The histograms of k_{in} for (a) case 1, (b) case 2, (c) case 3 for the tumor region (light gray) and outside (blue/dark gray) the tumor region (as indicated by circular/elliptical regions). The solid lines in figures show the Gaussian fit.

a bulk concentration value for each time instant. We then formed a time curve for the bulk ICG concentrations. Next, we fit the two-compartment model to the resulting time curves and estimated the bulk pharmacokinetic rates. Table 4 tabulates the bulk pharmacokinetic rates
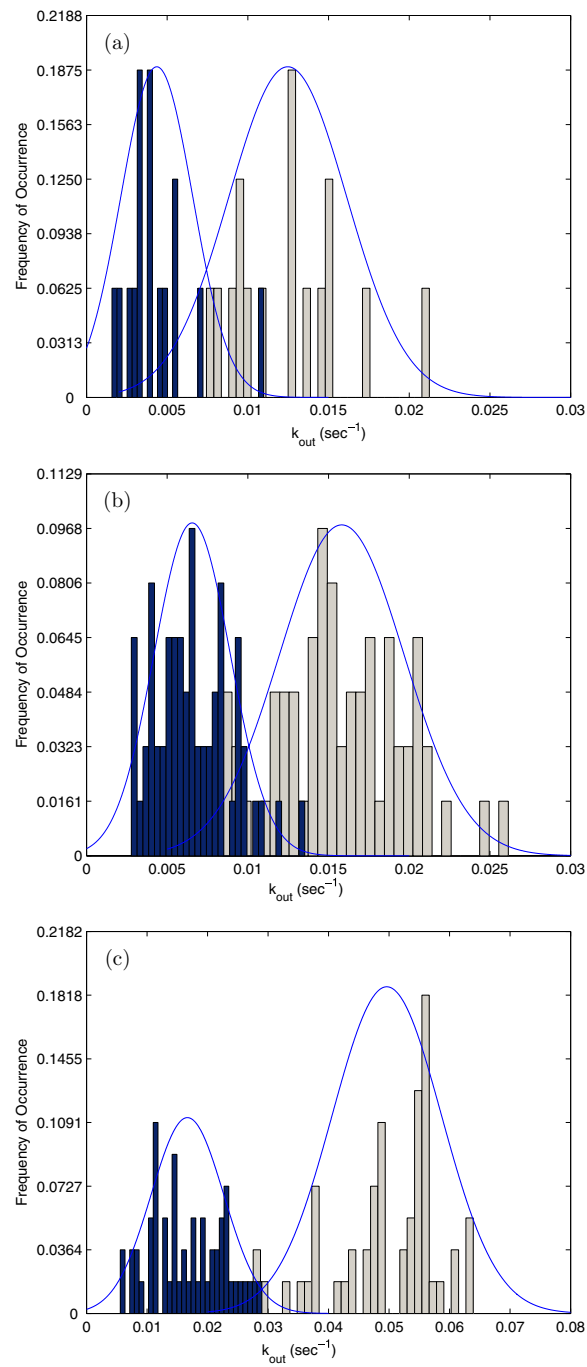
Figure 16. The histograms of k_{out} for (a) case 1, (b) case 2, (c) case 3 for the tumor region (light gray) and outside (blue/dark gray) the tumor region (as indicated by circular/elliptical regions). The solid lines in figures show the Gaussian fit.

for each patient. To compare the bulk rates with spatially resolved rates, in figures 17 and 18, the bulk pharmacokinetic rates are overlaid on the histograms of the pharmacokinetic rate
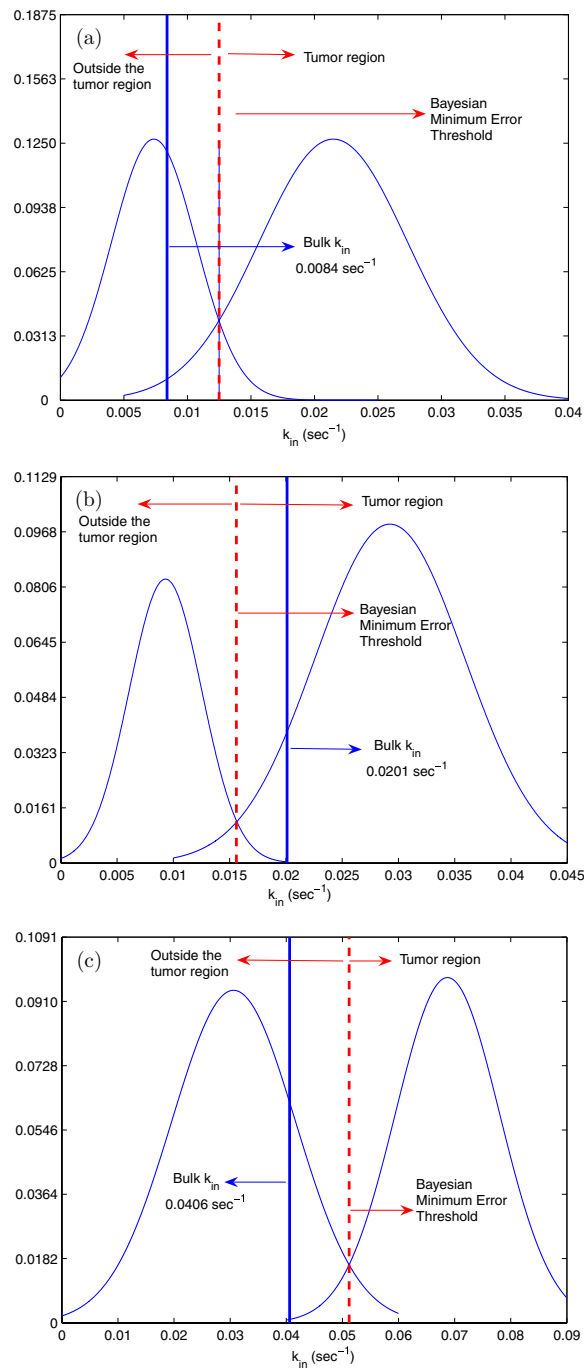
Figure 17. Solid lines (blue) shows bulk k_{in} rates for (a) case 1, (b) case 2, (c) case 3 together with the histogram fits. The dashed (red) line indicates the Bayesian minimum error classifier threshold.

images. The dotted line shows the Bayesian minimum error classifier threshold (the value corresponding to the intersection of the histograms) (Fukunaga 1990) for each case. We see
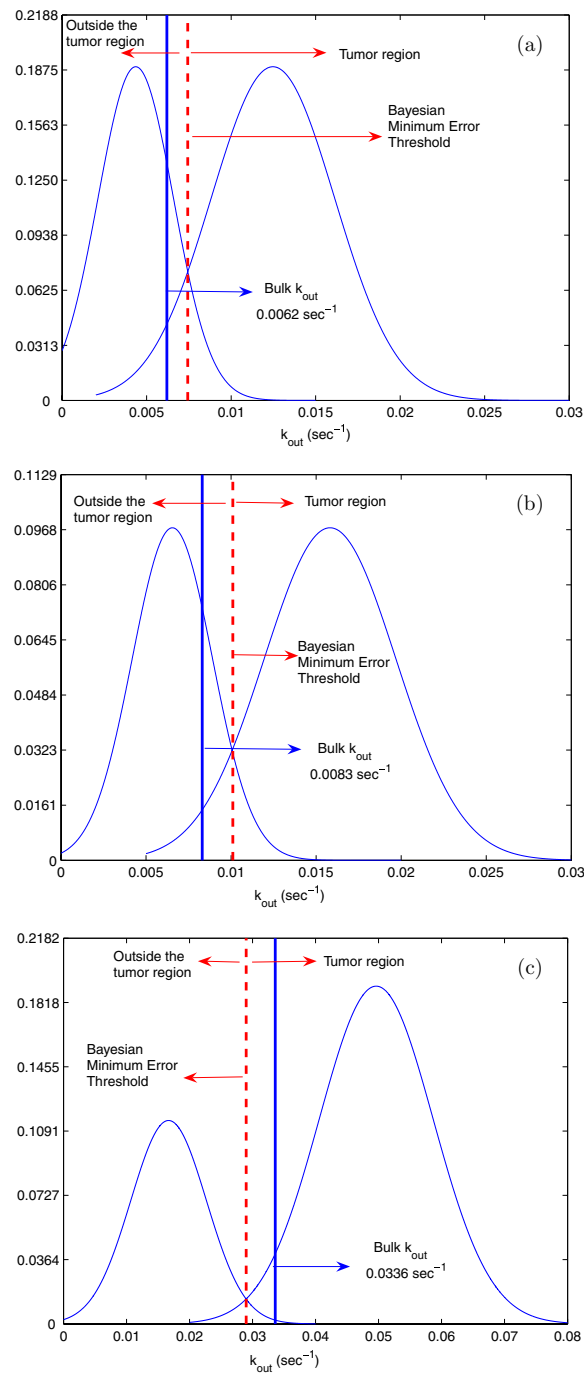
Figure 18. Solid lines (blue) shows bulk k_{out} rates for (a) case 1, (b) case 2, (c) case 3 together with the histogram fits. The dashed (red) line indicates the Bayesian minimum error classifier threshold.

that for case 1, the bulk rates of k_{in} and k_{out} are both classified as healthy tissue (outside the tumor region). For case 2, k_{in} is classified as cancerous tissue (in the tumor region) and k_{out} is

classified as healthy tissue. Similarly for case 3, k_{in} is classified as healthy and k_{out} is classified as cancerous tissue. This indicates that spatially resolved rates may provide more consistent and superior information than the bulk rates.

5. Conclusion

In this study, we presented a method of forming pharmacokinetic-rate images and reported pharmacokinetic rate images of ICG for three patients with breast tumors. To form pharmacokinetic rate images, we first obtained a sequence of ICG concentration images using the differential diffuse optical tomography technique. We next employed the two-compartment model, and estimated the pharmacokinetic rates and concentrations in each compartment for each voxel using the EKF framework. We have shown in our prior work (Alacam *et al* 2006) that the EKF framework has a number of advantages in pharmacokinetic rate estimation, some of which include robust estimation in the presence of measurement noise and dynamic model uncertainties.

We formed the pharmacokinetic rate images using the *in vivo* data obtained from three patients with breast tumors. We also obtained bulk pharmacokinetic rates for each patient. Both spatially resolved and bulk rates show that high values of k_{in} and k_{out} may be indicative of tumor aggressiveness. Along with the pharmacokinetic rates, we also estimated the ICG concentrations in plasma and EES compartments. We observed that ICG concentrations in plasma and the EES compartments are higher in the tumor region agreeing with the hypothesis that around the tumor region ICG may act as a diffusible extravascular flow in leaky capillary of tumor vessels.

Comparison of spatially resolved and bulk ICG pharmacokinetic rates show that ICG pharmacokinetic imaging may provide more consistent and superior information than bulk ICG pharmacokinetic rates.

While the available patient data are limited to perform a full scale receiver operating characteristic study, clearly, pharmacokinetic rate imaging provides a new tool to investigate and improve breast cancer diagnosis, staging, and treatment monitoring. This includes extraction of new quantitative features from ICG pharmacokinetic rate images, within patient comparison of these features, and statistical analysis of spatial distribution of pharmacokinetic rates. We leave for future work to collect sufficient number of patient data, and to fully investigate the value of ICG pharmacokinetic rate imaging for breast cancer diagnosis, staging, and treatment monitoring.

References

Alacam B, Yazici B, Intes X and Chance B 2006 Extended Kalman filtering for the modeling and analysis of ICG pharmacokinetics in cancerous tumors using NIR optical methods *Trans. IEEE Biomed. Eng.* **53** 1861–71
Anderson D H 1983 *Lecture Notes in Biomathematics: Compartmental Modeling and Tracer Kinetics* (Berlin: Springer)
Arridge S R 1999 Optical tomography in medical imaging *Inverse Problems* **15** 41–93

Boas D, Gaudette T and Arridge S 2001 Simultaneous imaging and optode calibration with diffuse optical tomography *Opt. Exp.* **8** 263–70

Boppart S A, Luo W, Marks D L and Singletary K W 2004 Optical coherence tomography: feasibility for basic research and image-guided surgery of breast cancer *Breast Cancer Res. Treat.* **84** 85–97

Chen C 1999 *Linear System Theory and Design* (New York: Oxford University Press)

Cuccia D J, Bevilacqua F, Durkin A J, Merritt S, Tromberg B J, Gulsen G, Yu H, Wang J and Nalcioglu O 2003 *In vivo* quantification of optical contrast agent dynamics in rat tumors by use of diffuse optical spectroscopy with magnetic resonance imaging coregistration *Appl. Opt.* **42** 2940–50

ElDeosky A, Seifalian A, Cope M, Delpy D and Davidson B 1999 Experimental study of liver dysfunction evaluated by direct indocyanine green clearance using near infrared spectroscopy *Br. J. Surg.* **86** 1005–11

Fukunaga K 1990 *Introduction to Statistical Pattern Recognition* (New York: Academic)

Gu X, Zhang Q, Larcom L and Jiang H 2004 Three-dimensional bioluminescence tomography with model-based reconstruction *Opt. Exp.* **12** 3996–4000

Gurfinkel M *et al* 2000 Pharmacokinetics of ICG and HPPH-car for the detection of normal and tumor tissue using fluorescence, near-infrared reflectance imaging: a case study *Photochem. Photobiol.* **72** 94–102

Hansen D, Spence A, Carski T and Berger M 1993 Indocyanine green (ICG) staining and demarcation of tumor margins in a rat glioma model *Surg. Neurol.* **40** 451–6

Hansen P and O'Leary D 1993 The use of the *L*-curve in the regularization of discrete ill-posed problems *SIAM J. Sci. Comput.* **14** 1487–503

Intes X and Chance B 2005 Non-PET functional imaging techniques: optical *Radio. Clin. North Am.* **43** 221–34

Intes X, Ripoll J, Chen Y, Nioka S, Yodh A G and Chance B 2003 *In vivo* continuous-wave optical breast imaging enhanced with indocyanine green *Med. Phys.* **30** 1039–47

Jacquez J A 1972 *Compartmental Analysis in Biology and Medicine: Kinetics of Distribution of Tracer-labeled Materials* (New York: Elsevier)

Landsman M L J, Kwant G, Mook G A and Zijlstra W G 1976 Light-absorbing properties, stability, and spectral stabilization of indocyanine green *J. Appl. Physiol.* **40** 575–83

Ljung L 1979 Asymptotic behavior of the extended Kalman filter as a parameter estimator for linear systems *IEEE Trans. Auto. Control* **AC24** 36–50

Mahmood U, Tung C H, Bogdanov Jr A and Weissleder R 1999 Near infrared optical imaging of protease activity for tumor detection *Radiology* **213** 866–70

Milstein A B, Webb K J and Bouman C A 2005 Estimation of kinetic model parameters in fluorescence optical diffusion tomography *J. Opt. Soc. Am.* **22** 1357–68

Mussurakis S, Buckley D L, Drew P J, Fox J N, Carleton P J, Turnbull L W and Horsman A 1997 Dynamic MR imaging of the breast combined with analysis of contrast agent kinetics in the differentiation of primary breast tumours *Clin. Radiol.* **52** 516–26

Nelson L and Stear E 1976 The simultaneous on-line estimation of parameters and states in linear systems *IEEE Trans. Auto. Control* **21** 94–8

Nioka S, Yung Y, Schnall M, Zhao S, Orel S, Xie C, Chance B and Solin S 1997 Optical imaging of breast tumor by means of continuous waves *Adv. Exp. Med. Biol.* **411** 227–32

Ntziachristos V, Chance B and Yodh A 1999 Differential diffuse optical tomography *Opt. Exp.* **5** 230–42

Ntziachristos V, Yodh A G, Schnall M and Chance B 2000 Concurrent MRI and diffuse optical tomography of breast after indocyanine green enhancement *Med. Sci.* **97** 2767–72

O'Leary M 1996 Imaging with diffuse photon density waves *PhD Thesis* Department of Physics & Astronomy, University of Pennsylvania

Ripoll J, Ntziachristos V, Carminati R and Nieto-Vesperinas M 2001a Kirchhoff approximation for diffusive waves *Phys. Rev.* **64** 051917

Ripoll J, Ntziachristos V, Culver J P, Pattanayak D N, Yodh A G and Nieto-Vesperinas M 2001b Recovery of optical parameters in multiplelayered diffusive media: theory and experiments *J. Opt. Soc. Am.* A **18** 821–30

Sevick-Muraca E M, Lopez G, Troy T L, Reynolds J S and Hutchinson C L 1997 Fluorescence and absorption contrast mechanisms for biomedical optical imaging using frequency-domain techniques *Photochem. Photobiol.* **66** 55–64

Shinohara H, Tanaka A, Kitai T, Yanabu N, Inomoto T, Satoh S, Hatano K, Yamaoka Y and Hirao K 1996 Direct measurement of hepatic indocyanine green clearance with near-infrared spectroscopy: separate evaluation of uptake and removal *Hepatology* **23** 137–44

Su M Y, Yu H J, Carpenter P M, McLaren C E and Nalcioglu O 2005 Pharmacokinetic parameters analyzed from MR contrast enhancement kinetics of multiple malignant and benign breast lesions detected in the same patients *Technol. Cancer Res. Treat.* **4** 255–63

Sun H, Collins J M, Mangner T J, Muzik O and Shields A 2006 Imaging the pharmacokinetics of [F-18]FAU in patients with tumors: PET studies *Cancer Chemother. Pharmacol.* **57** 343–8

Togneri R and Deng L 2003 Joint state and parameter estimation for a target-directed nonlinear dynamic system model *IEEE Trans. Sig. Proc.* **51** 3061–70

Tornoe C W 2002 Grey-box PK/PD modeling of insulin *MS Thesis* Technical University of Denmark

Vaupel P, Schlenger K, Knoop C and Hockel M 1991 Oxygenation of human tumors: evaluation of tissue oxygen distribution in breast cancers by computerized O_2 tension measurements *Cancer Res.* **51** 3316–22

Yodh A and Chance B 1995 Spectroscopy and imaging with diffusing light *Phys. Tod.* **48** 34–40